CHAPTER
THREE

SPECTRAL ELEMENT METHODS FOR UNSTEADY FLUID FLOW AND HEAT TRANSFER IN COMPLEX GEOMETRIES: METHODOLOGY AND APPLICATIONS

C.H. Amon

1 INTRODUCTION

Computational Heat Transfer (CHT) has experienced exceptional advances due to the improved computer hardware combined with the development of advanced numerical techniques and algorithms over the last decade. Numerical simulation has emerged as an alternative and, sometimes, as the only approach to analyze in detail, complex thermal-fluid phenomena. However, CHT is still at the stage of intensive development, particularly in engineering applications, where most of the problems considered in the past involve significant simplifications regarding geometry, physics and parameter range. Many computational techniques for thermal-fluid problems have been proposed, tested, and refined, mainly for steady flow and time-averaged conservation laws, the latter for modeling transport phenomenon in turbulent flows. Recently, there has been an increasing trend toward simulation of more complex thermal-fluid phenomena with a level of complexity that is close to industrial applications. CHT is therefore becoming an emerging field, not only in fundamental research, but also as a design and analysis tool in engineering practice [1, 2].

The ability to simulate complex-geometry and complex-physics flows has grown rapidly in the last two decades because of the effort devoted to Computational Fluid Dynamics (CFD). In the zeroth-order approach to convective heat transfer, the temperature field is solved in the presence of a known velocity field, i.e., uncoupled momentum and energy equations. Since the velocity field is seldom known, the flowfield needs to be obtained first, making CFD an essential part of CHT. The numerical prediction of convective heat transfer usually requires the combined solution of the velocity and temperature fields that are governed by the equations of conservation of momentum, mass, and energy. Often, simplifying assumptions or models are necessary to make complicated problems tractable. However, if a fairly complete and accurate mathematical description of the main factors affecting the transport phenomena are retained, and the numerical algorithms are suitable to solve the mathematical equation, then the results can be considered an accurate computer simulation of the physical process. Therefore, there are two different issues to consider regarding the analysis of numerical uncertainties: first, the quantification of the mathematical modeling errors, and, second, the identification and estimation of the numerical errors of the computational scheme used to solve the governing equations modeling the physical phenomenon.

We can broadly classify the numerical schemes used for simulating thermal-fluid phenomena into Eulerian and Lagrangian schemes with regards to formulation and into spectral, finite difference, finite volume, boundary-element and finite element techniques with regards to discretization algorithms. These schemes vary in complexity, computing efficiency, numerical accuracy, and flexibility. Each numerical method offers different advantages and limitations for simulating a certain class of transport phenomena. However, no one technique appears to be superior in solving a broad range of problems. Although most of these widely used numerical schemes fall within one of these categories and their differences might have been initially quite clear, recent approaches have combined these traditional schemes, leading to hybrid algorithms with encouraging results for solving complex thermal-fluid phenomena as well as for effective utilization of modern computer architecture. Several hybrid methods have been proposed using high-order polynomial expansions local to finite element, called *p* or combined *h-p* finite elements [3], global elements [4, 5] and spectral elements [6-9].

In this chapter, we concentrate on a class of hybrid discretization, called spectral element method, which combines finite elements and spectral schemes to produce high-order spatial accuracy. Both approaches are based on the principle of weighted residuals, and the spectral element method utilizes variational projection operators in conjunction with local Chebyshev or Legendre polynomial expansions which exhibit exponential convergence to smooth solutions. Even though other polynomial series can be employed, Chebyshev and Legendre polynomials are most frequently used because they are complete orthogonal sets of eigenfunctions which come from the solution of Sturm-Liouville problems. Furthermore, their coefficients are easily evaluated with a recurrence formula. The spectral element method can also be classified as a domain decomposition technique that combines globally unstructured and locally structured spatial discretizations. The global decomposition in macroelements provides geometric flexibility, and the local structure permits an efficient high-order approximation by spectral expansions through Chebyshev collocation points.

2 MATHEMATICAL FORMULATION

We consider unsteady incompressible flows and forced convection in three-dimensional domains which are governed by the Navier-Stokes, mass conservation and energy equations. We denote by $D = D_f \cup D_s$ the three-dimensional computational domain, and by ∂D the computational boundary surfaces, composed of solid heat conductive walls, $\partial D_{s\text{-}f} = \partial D_f \cup \partial D_s$, and periodic surfaces, ∂D_p. The governing dimensionless equations for fluid flow, conjugate conduction/convection heat transfer with a volumetric heat source, and mass transfer is given by a system of partial differential equations for the solid and fluid domains written in the following form:

$$\frac{\partial \overline{V}}{\partial t} = \overline{V} \times \omega - \nabla \tilde{\Pi} + \mathrm{Re}^{-1} \nabla^2 \overline{V} \tag{1}$$

$$\nabla \cdot \overline{V} = 0 \tag{2}$$

$$\frac{\partial T}{\partial t} = (\mathrm{Re} \cdot \mathrm{Pr})^{-1} \nabla^2 T - \overline{V} \cdot (\nabla T) + S \tag{3a}$$

$$\frac{\partial c}{\partial t} = (\mathrm{Re} \cdot Sc)^{-1} \nabla^2 c - \overline{V} \cdot \nabla c \qquad \text{in D} \tag{3b}$$

where $\overline{V}(\overline{x},t) = u\hat{x} + v\hat{y} + w\hat{z}$ is the velocity; $\overline{x}$ and t represent space and time, respectively; $\tilde{\Pi} = p + 1/2\, V^2$ is the dynamic pressure, $T(\overline{x},t)$ is the temperature field, and $\omega = \nabla \times \overline{V}$ is the vorticity, Re is the Reynolds number, Pr is the Prandtl number, and S corresponds to the nondimensional volumetric heat source; Sc is the Schmidt number and $c(\overline{x},t)$ is the concentration field. Buoyancy effects are considered negligible for the range of Reynolds numbers investigated, and viscous dissipation and radiation are likewise neglected in the energy equation. The boundary conditions for velocity in the Navier-Stokes equation are no-slip along the solid-fluid interfaces $\partial D_{s\text{-}f}$, and inflow/outflow or periodicity in the streamwise and spanwise directions. In the solid region D_s the velocities are zero in the energy equation and no-slip boundary conditions are satisfied. The appropriate boundary conditions will be discussed in the context of the individual applications presented in the later sections.

For periodic streamwise conditions and solid walls, the velocity boundary conditions are

$$\overline{V}(\overline{x},t) = 0 \qquad \text{on } \partial D_s \tag{4}$$

$$\overline{V}(x + nL, y, z, t) = \overline{V}(x, y, z, t) \qquad \text{on } \partial D_p \tag{5}$$

where L is the geometric periodicity and n an integer periodicity index. For the pressure we require

$$\tilde{\Pi}(\bar{x},t) = -\mathrm{f}(t)x + \Pi(\bar{x},t) \tag{6}$$

$$\Pi(x+nL,y,z,t) = \Pi(x,y,z,t) \tag{7}$$

where f(t) is the driving pressure gradient. Since in complex geometry flows or transitional flows the pressure gradient is unknown, it is preferable to impose the volume flow rate Q(t) as

$$\mathrm{Q}(t) = \int_{-\mathrm{W}}^{\mathrm{W}} \int_{\partial \mathrm{D}_{\mathrm{Bottom}}}^{\partial \mathrm{D}_{\mathrm{Top}}} u(x_0,y,z,t)\,dy\,dz \tag{8}$$

where 2W is the length in the spanwise direction.

For the forced convective heat transfer equation in the fluid domain $\mathrm{D_f}$, the temperature boundary conditions can be either Dirichlet (temperature), Neumann (flux), mixed Robin (heat transfer coefficient), periodicity, or continuity of temperature and heat flux for conjugate conduction/convection problems.

Simplified thermal modeling procedures often reduce a forced convective problem to solving the heat equation within the solid domain $\mathrm{D_s}$ and imposing the convective effects of the fluid through a heat transfer boundary condition at the solid-fluid interface *s-f*, Eq. (9).

$$h\left(T_{\mathrm{s-f}} - T_{\mathrm{ref}}\right) = -k_{\mathrm{s}}\frac{\partial T_{\mathrm{s}}}{\partial \hat{n}} \tag{9}$$

where h is the convective heat transfer coefficient and is a proportionality constant that models the ability of the fluid to remove heat at the solid-fluid interface. The proper reference temperature T_{ref} is problem-dependent and can be chosen as the ambient, bulk, adiabatic, or inlet temperatures. Reformulation of the problem necessitates that the heat transfer coefficient be obtained either empirically or numerically by solving the coupled system of Eqs. (1)-(3) only in the fluid domain $\mathrm{D_f}$ and imposing thermal boundary conditions along the solid-fluid boundary. This implies that the effect of heat conduction within the solid is replaced by idealized boundary conditions that assume the heat flow paths in the solid and decouple the resistance associated with conduction within the solid and convection within the fluid. However, in conjugate problems, neither the temperature nor the heat flux at the solid-fluid interface can be prescribed accurately a priori, especially in systems that involve intense heat transfer, multimaterial solid domains, and localized heat generation [10]. Therefore, the convective boundary condition, as previously described, may not provide accurate predictions. The appropriate thermal boundary conditions for conjugate conduction/convection [11] are continuity of heat flux and temperature at the solid-fluid interface and are termed boundary conditions of the fourth kind, Eqs. (10a)-(10b).

$$k_{\mathrm{s}} \frac{\partial T_{\mathrm{s}}}{\partial \hat{n}} = k_{\mathrm{f}} \frac{\partial T_{\mathrm{f}}}{\partial \hat{n}} \tag{10a}$$

$$T_{\mathrm{s}_{s-f}} = T_{\mathrm{f}_{s-f}} \tag{10b}$$

Different numerical techniques have been implemented to investigate conjugate conduction/convection and to demonstrate the effect of conjugation on thermal performance characteristics. However, most of the situations analyzed have been steady state with homogeneous solid domains and simple geometries. A two-dimensional steady conjugate study in a laminar boundary layer with a heat source at the solid-fluid interface was conducted using finite differences [12]. The time-dependent conjugate behavior of a semi-infinite slab exposed to uniform surface heating was studied using the unsteady surface element method [13]. The two-dimensional conjugate behavior of hydrodynamically, fully developed, laminar flow through a circular tube with thick walls and a finite heated length was investigated using a finite volume approach [14]. A semi-analytical approach that utilizes an integral formulation for the fluid domain and a finite volume formulation for the solid domain was successfully developed to study plates with discrete heat sources, which model surface-mounted electronic packages [15]. Mixed laminar convection from local heat-generating components was also studied using a simpler-based approach [16]. Time-dependent studies of multimaterial, local heat generating configurations using the spectral element method were conducted by Nigen and Amon [17, 18] for both laminar and transitional Reynolds numbers. This investigation contrasted thermal behavior characteristics for conjugate and convection-only representations of a simulated electronic package and demonstrated the significance of including time-dependency and conjugation.

3 DISCRETIZATION

3.1 Temporal Discretization

The time-discretization procedure consists of a fractional scheme for the semidiscrete formulation of the time-dependent term in the Navier-Stokes, energy and concentration equations. Intermediate velocities $\hat{V}$ and $\hat{\hat{V}}$, Eqs. (11)-(13), and temperature $\hat{T}$, Eqs. (16)-(17) are computed in a way that the left-hand side yields $\partial \overline{V} / \partial t$ whereas the right-hand side contains the contributions of the nonlinear, pressure, and viscous terms. The advantage of this time-splitting scheme is that it reduces the coupled system of Eqs. (1) and (2) into a system of separately solvable equations for the pressure and velocity enabling the application of different algorithms to different terms in the Navier-Stokes equations to obtain gains in efficiency. The error, due to the time-splitting scheme, scales as $[o(\Delta t^2)+ o(\Delta t/\mathrm{Re})]$ and restricts the time-step size in applications seeking to simulate time-dependent transitional flows. The nonlinear convective term, Eq. (11), is treated explicitly to decrease the computer time required per step because of the need to solve a nonlinear problem at each time step. The viscous term, Eq. (13), is treated implicitly to avoid unreasonable time-step restrictions due to the stiffness of diffusion problems [5] and the high resolution of Chebyshev spectral approximations near the boundary of the elements [19]. The dynamic pressure Π is calculated in Eq. (14) so that the velocity satisfies the incompressible condition of Eq. (2) even though Π does not appear in this equation. The time-stepping procedure is given by the following steps:

Nonlinear step:

$$\frac{\hat{V}^{n+1} - \overline{V}^{n}}{\Delta t} = \sum_{i=0}^{2} \beta_i \left(\overline{V}^{n-i} \times \omega^{n-i}\right) + f \qquad \text{in D} \tag{11}$$

Pressure step:

$$\frac{\hat{\hat{V}}^{n+1} - \hat{V}^{n+1}}{\Delta t} = -\nabla \Pi \qquad \text{in D} \tag{12a}$$

$$\nabla \cdot \hat{\hat{V}}^{n+1} = 0 \qquad \text{in D} \tag{12b}$$

$$\hat{\hat{V}} \cdot \hat{n} = 0 \qquad \text{on } \partial\text{D} \tag{12c}$$

Viscous step:

$$\frac{\overline{V}^{n+1} - \hat{\hat{V}}^{n+1}}{\Delta t} = \frac{1}{\mathrm{Re}} \nabla^2 \overline{V}^{n+1} \qquad \text{in D} \tag{13}$$

where the superscript *n* refers to time step. The first step, Eq. (11) represents the explicit treatment of the nonlinear convective term by a third order Adams-Bashforth method, where the coefficients are $\beta_0 = 23/12$, $\beta_1 = -16/12$, and $\beta_2 = -5/12$. This scheme introduces low dispersion errors and contains a relatively large portion of the imaginary axis within the absolute stability region of the scheme.

In the second step, Eqs. (12a)-(12c), the effect of the pressure is included and incompressibility is satisfied. By taking the divergence of Eq. (12a) and imposing Eq. (12b), we obtain the following Poisson equation for the pressure:

$$\nabla^2 \Pi = \nabla \cdot \frac{\hat{V}^{n+1}}{\Delta t} \quad \text{in D} \tag{14a}$$

This elliptic equation is then solved implicitly subject to

$$\nabla \Pi \cdot \hat{n} = \frac{\hat{V}^{n+1} \cdot \hat{n}}{\Delta t} \quad \text{on } \partial \mathrm{D}_s \tag{14b}$$

The imposition of an inviscid-type boundary condition, proposed first by Deville and Orszag [19], introduces errors of $o(\Delta t/\mathrm{Re})$ that are important only at very low Reynolds number flows.

Finally, at the third fractional step, for the Navier-Stokes equation, Eq. (13), the viscous corrections are handled implicitly using a Crank-Nicolson scheme and the no-slip boundary conditions are imposed, giving

$$\left(\nabla^2 - \frac{2}{\Delta t}\mathrm{Re}\right)\left(\bar{V}^{n+1} + \bar{V}^{n}\right) = -\frac{2}{\Delta t}\mathrm{Re}\left(\hat{V}^{n+1} + \bar{V}^{n}\right) \quad \text{in D} \tag{15}$$

The nonlinear convective term, treated explicitly, is the only source that imposes stability conditions for the scheme (Courant-Friedrech-Lewy condition number), since the pressure and viscous contributions are treated implicitly by Euler backward or Crank-Nicolson schemes, which are unconditionally stable, resulting in an efficient and robust inversion of the global system matrices. Consequently, the time-step size is constrained by both accuracy in the time-splitting formulation and stability of the explicit scheme. For high Reynolds number flows in the turbulent flow regime, the viscous term can be treated explicitly since stability conditions for the convective contributions, Eq. (11), are as severe as the ones for the diffusive contributions, Eq. (13).

For the energy and mass transfer equation, Eqs. (3a)-(3b), we use a similar semi-implicit time-stepping scheme with two steps. The first step is an explicit third-order Adams-Bashforth step for the convective and source volumetric heat generation terms, and the second step is an implicit Crank Nicolson step for the conductive terms. The semi-discrete equations for $T^{n}(x) = T(x, n\Delta t)$ are then

$$\hat{T}^{n+1} - T^{n} = -\Delta t \sum_{q=0}^{2} \beta_q \nabla \cdot (\bar{V}T)^{n-1} + S \tag{16}$$

$$T^{n+1} - \hat{T}^{n+1} = -\frac{\Delta t}{2\mathrm{Re}\cdot Pr}\left[\nabla^2 (T^{n+1} + T^{n})\right] \tag{17}$$

and boundary conditions are imposed on Eq. (17).

The numerical approach consists of integrating the continuity and Navier-Stokes equations for the fluid portion of the domain and then integrating the energy and mass transfer equations for both the solid and fluid domains. This procedure is iterated in time until either an asymptotically-steady, time-periodic or converged state is reached.

3.2 Multi-dimensional Spatial Discretization

Once we obtain the semidiscrete temporal equations, we proceed with the spatial discretization using a spectral element-Fourier decomposition of the three-dimensional computational domain. For a homogeneous geometry in the z direction, periodic boundary conditions and symmetry are consistent with the governing equations (1) and (2). Therefore, the velocity and pressure can be represented as two-dimensional *(x,y)* components with Fourier expansions in the homogeneous z direction,

$$\begin{bmatrix} u(x,t) \\ v(x,t) \\ w(x,t) \\ \Pi(x,t) \end{bmatrix} = \begin{bmatrix} u^{(2)}(x,y,t) \\ v^{(2)}(x,y,t) \\ w^{(2)}(x,y,t) \\ \Pi^{(2)}(x,y,t) \end{bmatrix} + \sum_{\mathrm{m}=1}^{\mathrm{M}} \begin{bmatrix} u_{\mathrm{m}}(x,y,t)\cos(\mathrm{m}\beta z) \\ v_{\mathrm{m}}(x,y,t)\cos(\mathrm{m}\beta z) \\ w_{\mathrm{m}}(x,y,t)\sin(\mathrm{m}\beta z) \\ \Pi_{\mathrm{m}}(x,y,t)\cos(\mathrm{m}\beta z) \end{bmatrix} \tag{18}$$

where β is the wave number in the spanwise direction. We use cosine and sine expansions instead of exponentials because of the symmetry in the z direction and the reality conditions of the velocity and pressure in the physical space. For the analysis of two-dimensional flows, the v_{m} are identically zero; for linear three-dimensional stability analysis, a single infinitesimally small spanwise mode is included; and for three-dimensional flows, M is chosen so as to include all excited spanwise scales.

To impose the flow-rate condition Q*(t)* in Eq. (8), let us assume for simplicity the flow direction to be the x direction. Then, for incompressible flow, at station x_0,

$$\begin{aligned} \mathrm{Q}(t) &= \iint u(x_0,y,t)\,dydz = \iint \left[u^{(2)}(x_0,y,t) + \sum_{\mathrm{m}=1}^{\mathrm{M}} u_{\mathrm{m}}(x_0,y,t)\cos(\mathrm{m}\beta z) \right] dydz \\ &= \iint u^{(2)}(x_0,y,t)\,dydz + \sum_{\mathrm{m}=1}^{\mathrm{M}} \int u_{\mathrm{m}}(x_0,y,t)\,dy \int \cos(\mathrm{m}\beta z)\,dz \end{aligned} \tag{19}$$

where

$$\int_{-\mathrm{W}}^{\mathrm{W}} \cos(\mathrm{m}\beta z)\,dz = 0, \qquad \mathrm{m} \neq 0$$

Therefore, only the mean streamwise velocity $u^{(2)}$ contributes to the net flow rate, obtaining

$$Q(t) = 2W\int_{\partial D_{Bottom}}^{\partial D_{Top}} u^{(2)}(x_0,y,t)\,dy = Q_{2D}(t)\cdot 2W \tag{20}$$

It suffices to impose at any x_0 station

$$Q_{2D}(t) = \int_{\partial D_{Bottom}}^{\partial D_{Top}} u^{(2)}(x_0,y,t)\,dy \tag{21}$$

which is done in a preprocessing stage, before the time-stepping procedure.

3.2.1 Fourier expansions. The Fourier expansions, Eq. (18), are then inserted into the semidiscrete equations, Eqs. (11), (14), and (15). To demonstrate this procedure, we consider the elliptic operator corresponding to the pressure step, Eq. (14a), and substituting Eq. (18), we obtain

$$\sum_{m=1}^{M}(\nabla^2 - m^2\beta^2)\Pi_m \cos(m\beta z) = \frac{1}{\Delta t}\left(\sum_{m=1}^{M}\frac{\partial \hat{u}_m}{\partial x} + \frac{\partial \hat{v}_m}{\partial y} + m\beta\hat{w}_m\right)\cos(m\beta z) \tag{22}$$

where $\nabla^2 = \partial^2/\partial x^2 + \partial^2/\partial y^2$ and Π_m are the Fourier coefficients for the spanwise direction. First, we follow a Galerkin approach in z, multiplying Eq. (22) by cos(kβz), integrating and applying orthogonality property to obtain the following equation for the Fourier coefficients Π_m [20]:

$$\begin{gathered}(\nabla^2 - m^2\beta^2)\Pi_m = \frac{1}{\Delta t}\left(\frac{\partial \hat{u}_m}{\partial x} + \frac{\partial \hat{v}_m}{\partial y} + m\beta\hat{w}_m\right)\\ m = 1,2,\ldots,M\end{gathered} \tag{23}$$

We can now proceed to discretize the two-dimensional components of the velocity and pressure in the *x-y* plane using a variational spectral element discretization.

3.2.2 Spectral element discretization. In a two-dimensional spectral element discretization, the computational domain is partitioned into K non-overlapping four-sided macroelements given by $\Re^K = [a^K, b^K]$. Each element is then isoparametrically mapped from the physical $\bar{x} = (x, y)$ space to the local *(r,s)* coordinate system. The geometry, pressure, and velocity are represented as a tensor product of high-order Lagrangian interpolants through Gauss-Lobatto Chebyhev collocation points, defined as

$$\left[\bar{x},\bar{V},\Pi\right](r,s)=\sum_{k=1}^{K}\sum_{i=0}^{N_1}\sum_{j=0}^{N_2}(\bar{x},\bar{V},\Pi)_{ij}^{k}h_i(r)h_j(s) \tag{24}$$

where $h_i(r)$ and $h_j(s)$ are local Lagrangian interpolants that satisfy $h_i(\zeta_j)=\delta_{ij}$ at the local *(r,s)* coordinates, and δ_{ij} is the Kronecker delta symbol. The discrete space is defined in terms of the spectral element discretization parameters (K, N_1, N_2), where K is the number of spectral elements, and N_1 and N_2 are the degrees of the piecewise high-order polynomials in the *r* and *s* directions, respectively. Isoparametric mappings are used to transform general curvilinear domains into standard domains as illustrated in Fig. 1. To insure rapid convergence of the resulting expansions, the local and physical collocation points are chosen to be the Gauss-Lobatto Chebyshev points, defined as $x_j^i=-\cos\pi j/N^i$. Also, the choice of these collocation points results in closed-form analytical expressions for the quadratures involved in the computations. The Langrangian interpolants in Eq. (24) are expanded as

$$h_m(\zeta)=\frac{2}{N}\sum_{n=0}^{N}\frac{1}{\bar{c}_m\bar{c}_n}T_n(\zeta_m)T_n(\zeta) \tag{25}$$

where $m = i,j$ and $\zeta = r,s$, and T_n are the Chebyshev polynomials defined as

$$T_n(\cos\theta)=\cos n\theta \tag{26}$$

and

$$\bar{c}_m=\begin{cases}1 & m\neq 0,N\\ 2 & m=0,N\end{cases} \tag{27}$$

In the numerical simulations presented in this paper, we choose the same resolution in both spatial directions, i.e., $N = N_1 = N_2$. However, in practice, this does not need to be the case. For general complex geometry computational domains, we can extend the two-dimensional spectral element discretizations to three-dimensions by employing hexahedral spectral elements. An alternative approach for flows with one homogeneous or periodic direction consists in discretizing this direction through equally-spaced planes, using the Fourier expansions introduced in Section 3.2.1.

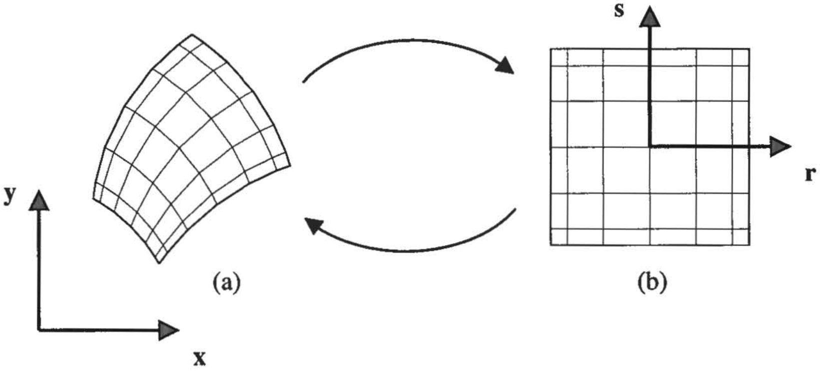

Figure 1 Four-sided spectral macroelement domain (a) curvilinear macroelement, and (b) standard spectral macroelement.

To illustrate the two-dimensional spectral element discretization, we consider Eq. (23) corresponding to the pressure step discretized by Fourier expansions in the spanwise direction. To simplify the notation, let us set $g=(\partial\hat{u}_{\mathrm{m}}/\partial x+\partial\hat{v}_{\mathrm{m}}/\partial y+\mathrm{m}\beta\hat{w}_{\mathrm{m}})/\Delta t$ where all of the variables are known from the nonlinear step calculations. Then, it can be written as a modified Helmholtz equation of the form

$$\begin{gathered}\left(\nabla^2-\mathrm{m}^2\beta^2\right)\Pi_{\mathrm{m}}=g \qquad \text{in D}\\ \mathrm{m}=1,\ldots,\mathrm{M}\end{gathered} \tag{29}$$

subject to homogeneous Dirichlet boundary conditions, $\Pi=0$ on $\partial\mathrm{D}$. Equation (29) is discretized using variational spectral elements in the *x-y* plane. The variational formulation recognizes the equivalence between solving the differential Eq. (29) and maximizing the functional

$$I_{\mathrm{m}}(\Pi)=\int_D\left[-\frac{1}{2}\nabla\Pi_{\mathrm{m}}\cdot\nabla\Pi_{\mathrm{m}}-\frac{\mathrm{m}^2\beta^2}{2}(\Pi_{\mathrm{m}})^2-\Pi_{\mathrm{m}}\,g\right]dA \tag{30}$$

The spectral element discretization corresponds to numerical quadrature of the variational form, Eq. (30), restricted to the discrete space defined in terms of the parameters ($\mathrm{K}, \mathrm{N}_1, \mathrm{N}_2$).

In local *(r-s)* coordinates, Eq. (30) is written as

$$I_{\mathrm{m}}(\Pi)=\sum_{\mathrm{k}=1}^{\mathrm{K}}\int_{-1}^{1}\int_{-1}^{1}\left(-\frac{1}{2}\frac{\hat{\nabla}\Pi\cdot\hat{\nabla}\Pi}{|J|}-\frac{|J|\mathrm{m}^2\beta^2}{2}\Pi^2-|J|\Pi g\right)drds \tag{31}$$

where Π corresponds to Π_m, J is the Jacobian of the elemental transformations, and $\hat{\nabla}$ is the conservative form of the Jacobian multiplied gradient operator [20].

To generate the discrete equations for each element k, we insert the interpolants Eq. (25) and the nodal collocation values of the geometric transformation into the functional. Then, we use a Galerkin-weighted residual technique and perform the resulting integrals, requiring stationarity at the collocation points. Using the selected Gauss-Lobatto Chebyshev collocation points ζ^k_{pq} and corresponding weights $\rho_{pq} = \rho_p \rho_q$, Eq. (31) is expressed as

$$\sum_{k=1}^{K}\sum_{p=0}^{N_1}\sum_{q=0}^{N_2} \rho_{pq} J^k_{pq} \left[\frac{\partial \Pi}{\partial x_j}\frac{\partial \Pi}{\partial x_j}\right]_{\zeta^k_{pq}} + m^2\beta^2 \sum_{k=1}^{K}\sum_{p=0}^{N_1}\sum_{q=0}^{N_2} \rho_{pq} J^k_{pq} \left[\Pi\Pi\right]_{\zeta^k_{pq}}$$
$$= -\sum_{k=1}^{K}\sum_{p=0}^{N_1}\sum_{q=0}^{N_2} \rho_{pq} J^k_{pq} \left[\Pi g\right]_{\zeta^k_{pq}} \tag{32}$$

The Jacobian J^k_{pq} of the transformation from physical to local coordinates is calculated from the partial derivatives of the geometric isoparametric transformation r_x, r_y, s_x, and s_y.

Once the local basis function is selected, the spectral element approximation for Π^k is

$$\Pi^k = \sum_{n=0}^{N_1}\sum_{m=0}^{N_2} \Pi^k_{mn} h_m(r) h_n(s), \qquad \forall_{m,n} \in (0,\ldots,N_1),\ (0,\ldots,N_2) \tag{33}$$

where Π^k_{mn} are the expansion coefficients and also the local nodal values of Π. The geometry is also represented via similar tensorial products with the same order polynomial degree, i.e.,

$$(x,y)^k = \sum_{n=0}^{N_1}\sum_{m=0}^{N_2} \left(x^k_{mn}, y^k_{mn}\right) h_m(r) h_n(s), \qquad \forall_{m,n} \in (0,\ldots,N_1),\ (0,\ldots,N_2) \tag{34}$$

where x^k_{mn} and y^k_{mn} are the global physical coordinates at the node (mn) in the k element.

To construct the discrete matrix of the global system, we insert Eq. (33) into Eq. (32) and perform direct stiffness summation [21] adding at the boundary nodes the contributions from the neighboring elements, obtaining

$$\sum_{k=1}^{K}{}'\sum_{m=0}^{N_1}\sum_{n=0}^{N_2} \left(\phi^k_{ijmn} + m^2\beta^2 J^k_{ij} B^k_{im} B^k_{jn}\right)\Pi^k_{mn} = -\sum_{k=1}^{K}{}'\sum_{m=0}^{N_1}\sum_{n=0}^{N_2} J^k_{ij} B^k_{im} B^k_{jn} g^k_{mn} \tag{35}$$

where $\sum'$ denotes direct stiffness summation, and

$$\phi^{k}_{mn} = \rho_{pq} J^{k}_{pq} [(r_x)^2_{pq} \mathcal{D}_{pi} \mathcal{D}_{pm} \delta_{nq} + (s_x)^2_{pq} \mathcal{D}_{qj} \mathcal{D}_{qn} \delta_{mp} + (r_x s_x)^2_{pq} \mathcal{D}_{pi} \mathcal{D}_{qn} \delta_{mp} +$$

$$(r_x s_x)_{pq} \mathcal{D}_{qj} \mathcal{D}_{qm} \delta_{nq}] \mathcal{D}_{ij} = \frac{\partial h_j}{\partial \zeta}(\zeta_i), \qquad B_{ij} = \int_{-1}^{1} h_i(\zeta) h_j(\zeta) d\zeta, \qquad \zeta = r, s \tag{36}$$

The spectral solutions are C^0 across the boundaries of the elements with interfacial continuity constraints imposed only by the variational formulation without requiring any explicit patching at the elemental interfaces. Therefore, there is a weak coupling between dependent variables for neighboring elements. This results in banded, relatively sparse matrices, which are critical regarding computational efficiency of the method in terms of memory requirements and processing time.

Adequate mesh resolution is verified by comparing the temperature, concentration and flow characteristics using different order of local expansions and/or macroelement discretizations. The control of spatial resolution and the high degree of accuracy associated with this technique makes it well-suited for studying conjugate problems with localized heat generation and multimaterial solid domains, especially those with large variation in material properties.

4 APPLICATIONS

In this section, we present direct numerical simulations of several time-dependent fluid flows including mass and heat transport.

4.1 Flows in Abdominal Aortic Aneurysms

The first example corresponds to relatively complicated steady and pulsatile axisymmetric flows with curvilinear boundaries encountered in abdominal aortic aneurysms. Abdominal Aortic Aneurysms (AAAs) are localized balloon-shaped expansions commonly found in the infrarenal segment of the abdominal aorta, between the renal arteries and the iliac bifurcation. While the cause and nature of AAAs is still an important matter of debate, abdominal aortic aneurysm rupture is the 15th leading cause of death in the United States, affecting patients over 55 years of age, typically 2-4% of elderly males. As the overall mortality rate following aneurysm rupture may exceed 90% [22] determining the risk factors that may have an important role in aneurysm growth and rupture has become an integrated multidisciplinary task oriented towards obtaining an agreement on the pathogenesis and evolution of AAAs. It is well known now that arterial diseases, present in local irregular geometries, are the result of a combination of complex biochemical processes that take place in the vascular wall at the cellular level as well as hemodynamic factors resulting from the interaction of blood flow and the endothelium, the innermost cellular monolayer of the cardiovascular system. Recent investigations related to AAA phenomena are based on four major areas: (i) clinical studies focused on the etiology and screening of AAAs, as well as the determination of possible risk factors related to chemical alterations occurring in the cellular matrix of the endothelium; (ii) experimental and numerical studies focused on the simulation of physiological hemodynamics in aneurysm models; (iii) experimental and numerical studies based on stress-strain analysis and wall mechanics of the aneurysm wall, and (iv) in-vitro cell biology investigations and numerical simulations of cell models that attempt to correlate the hemodynamic patterns found in arterial models with the clinical evidence known for arterial diseases. Several numerical studies of steady and pulsatile flows through aneurysms are found in the literature. Guzmán and Amon [23] and Amon, et al. [24] have utilized spectral element discretizations to study the temporal flow evolution of laminar, transitional and chaotic flows in converging-diverging channels using a geometry similar to that represented in Fig. 2. Direct numerical simulations of non-Newtonian flow through double-aneurysm models have been conducted under pulsatile conditions, resulting in flow patterns and wall shear stresses that were underestimated for otherwise Newtonian flow behavior [25, 26]. Validation of pulsatile non-Newtonian flow simulations has been done by means of three asymptotic cases that take into account geometric irregularities in the model [27]. Currently, Finol and Amon [28, 29] are performing spectral element simulations of blood flow through AAA models. The objective of these simulations is to provide new insights to hemodynamic indicators that have not yet been evaluated when quantifying disturbed flow conditions, both steady and pulsatile, at the aneurysm wall.

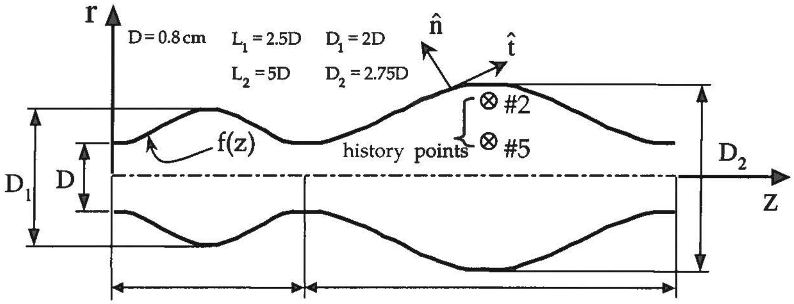

Figure 2 Representation of the axisymmetric model of the two-aneurysm abdominal aorta.

4.1.1 Mathematical formulation. The geometry of the abdominal aorta with two aneurysms is shown in Fig. 2. Two converging-diverging regions define this geometry, the physical model of which has been previously used by Guzmán, et al. [25, 27]. We consider both steady and pulsatile, incompressible, homogeneous, Newtonian flow in a two-aneurysm rigid-wavy-walled axisymmetric model. The deformed wall is represented by two sine functions as follows:

$$f(z)=\begin{cases}\left(\dfrac{\mathrm{D}_1-\mathrm{D}}{4}\right)\left[1+\sin\left(\dfrac{2\pi z}{\mathrm{L}_1}-\dfrac{\pi}{2}\right)\right]+\dfrac{\mathrm{D}}{2} & 0\leq z\leq \mathrm{L}_1\\[2ex] \left(\dfrac{\mathrm{D}_2-\mathrm{D}}{4}\right)\left[1+\sin\left(\dfrac{2\pi(z-\mathrm{L}_1)}{\mathrm{L}_2}-\dfrac{\pi}{2}\right)\right]+\dfrac{\mathrm{D}}{2} & \mathrm{L}_1\leq z\leq \mathrm{L}_2\end{cases}\tag{37}$$

The momentum and continuity equations in axisymmetric coordinates that govern these flows are given by

$$\rho\left(\frac{\partial u_z}{\partial t}+\overline{V}\cdot\nabla u_z\right)=-\frac{\partial p}{\partial z}+\left(\frac{\partial \tau_{zz}}{\partial z}+\frac{1}{r}\frac{\partial}{\partial r}(r\tau_{rz})\right)\tag{38a}$$

$$\rho\left(\frac{\partial u_r}{\partial t}+\overline{V}\cdot\nabla u_r\right)=-\frac{\partial p}{\partial r}+\left(\frac{\partial \tau_{rz}}{\partial z}+\frac{1}{r}\frac{\partial}{\partial r}(r\tau_{rr})\right)\tag{38b}$$

$$\frac{1}{r}\frac{\partial}{\partial r}(ru_r)+\frac{\partial u_z}{\partial z}=0\tag{38c}$$

where $\overline{V}(\overline{x},t)=u_r\hat{r}+u_z\hat{z}$ is the velocity vector, and τ_{zz}, τ_{rr} and τ_{rz} are the components of the two-dimensional stress tensor. The boundary conditions for the velocity $\overline{V}(\overline{x},t)$ are nonslip at the walls, symmetry at the centerline, fully developed parabolic profile at the inlet, and zero-traction outflow condition at the exit. Blood flow is simulated for average blood properties [30] with molecular viscosity $\mu = 0.00319$ Pa·s and density $\rho = 1{,}050$ kg/m^3. The governing equations are nondimensionalized by the factor D/2; hemodynamic parameters evaluated at the arterial wall are nondimensionalized using their corresponding magnitudes obtained for Poiseuille flow. The governing equations, subject to the appropriate boundary conditions, are solved numerically using a spectral element method for the spatial discretization with local Legendre polynomial expansions [6, 7].

The calculation of the local Wall Shear Stress Gradient (*WSSG*) is based on the predictor equation proposed by Lei and Kleinstreuer [31] at the cellular level, corrected from their previous work [32]:

$$WSSG = \sqrt{\left(\frac{\partial \tau_w}{\partial \hat{t}}\right)^2 + \left(\frac{\partial \tau_w}{\partial \hat{n}}\right)^2} \tag{39}$$

where $\hat{t}$ and $\hat{n}$ are the local tangential and normal directions to the wall, as shown in Fig. 2. The nondimensional *WSSG* is obtained using the factor $2\tau_{wo}/D$, which is the gradient of shear stress at the wall for Poiseuille flow:

$$WSSG^* = \frac{WSSG}{2\tau_{wo}/D} \tag{40}$$

4.1.2 Steady flow. Numerical results are obtained at Reynolds numbers over the range $10 \leq Re \leq 2265$. The Reynolds number is based on the undilated vessel diameter (diameter of the model at $z = 0$) and the average velocity at the entrance of the vessel. In the constant flow simulations, the inlet velocity profile is parabolic, corresponding to a fixed inlet flow rate. A time-dependent initial value code is used to find the solution for steady flow, starting from arbitrary initial conditions. The pressure at the exit of the two-aneurysm model is set to 70 mmHg, which is the time-average late diastolic pressure in the infrarenal segment of the human abdominal aorta [33]. Therefore, all the pressure results are relative to this value.

Typical laminar flow streamlines for the range of Reynolds number $10 \leq Re \leq 2265$ are shown in Fig. 3. At $Re = 10$, corresponding to a flow rate of 0.012 L/min, no flow separation occurs, and the main stream of fluid fills completely each of the vessel dilatations in a forward flow pattern. The converging-diverging shape of the model produces successive convective decelerations and accelerations of the flow that result in very small axial velocities near the wall at the center of each aneurysm. The onset of flow separation is found to occur within the range $24.74 < Re < 25.21$. For $Re = 25$, negative axial velocities in the order of magnitude of 10^{-5} cm/s are obtained close to the wall. Figures 3(b) through 3(f) show streamline plots that demonstrate a characteristic flow pattern: an inner core flow that passes through each dilation and two main surrounding regions of flow recirculation and separation. The symmetrically recirculating regions inside the arterial expansions are characterized by an upper subregion of reversed flow, which interacts with the AAA wall, and a lower subregion of forward flow which is sheared by the fluid core. For $Re \geq 500$, the fluid moving in reverse direction occupies most of the aneurysm sac volume, while the forward moving fluid in the vortex fills in a very small portion of the expansion. This is represented by a contraction of the streamlines in the distal half of each aneurysm, to the right and below the center of the vortex, and an expansion of the streamlines in the proximal half, especially close to the wall. Consequently, the upper subregion is essentially a zone of slowly moving particles of fluid, nearly stagnant, of high distal and low proximal shear due to blood flow-endothelium interaction. At each aneurysm enlargement, streamline separation occurs proximally. The dividing streamline represents particles of fluid that, after separation, continue flowing distally, along the undisturbed moving core. Particles traveling right above the dividing streamline enter the AAA sac, and upon reaching the distally located boundary layer reattachment point, reverse their direction, flowing backwards along the wall, towards the separation point. Therefore, fluid along the wall moves against a pressure gradient and after traveling the longitudinal perimeter of each aneurysm, the core flow, which is faster, separates from the wall and forms a laminar main stream with two or three annular regions of flow recirculation.

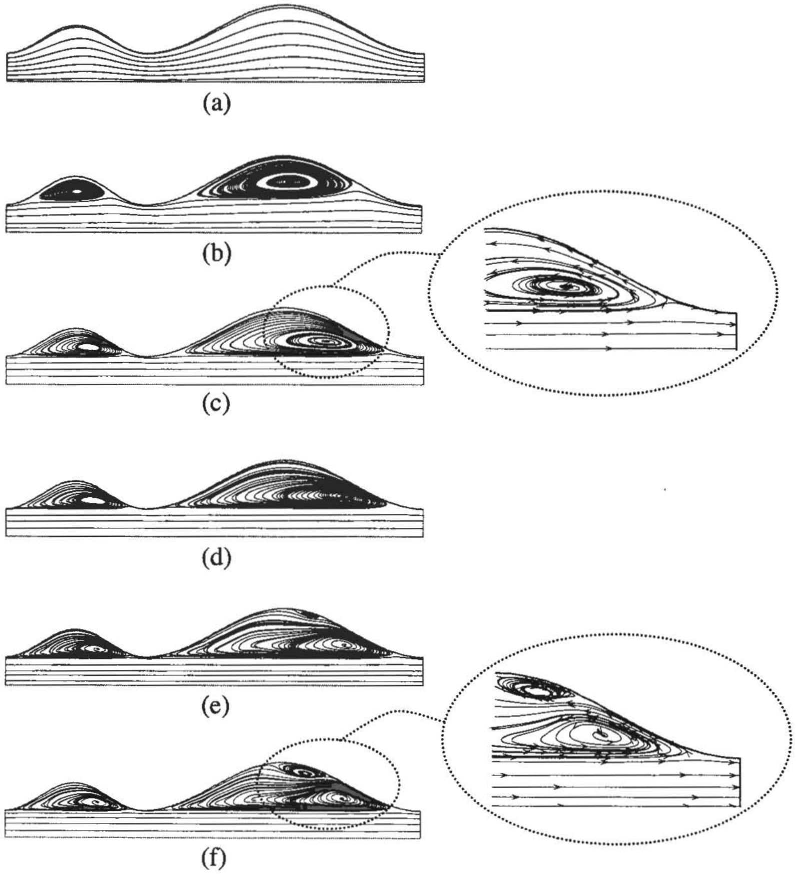

Figure 3 Streamlines for laminar steady flow at (a) Re = 10, (b) Re = 100, (c) Re = 500, (d) Re = 1000, (e) Re = 1750, and (f) Re = 2265. The direction of the flow is from left to right.

Figures 3(b) through 3(f) also show that as the Reynolds number is increased, the center of the recirculating flow regions moves downstream, distally, and also downward, closer to the main stream. This causes the displacement of the boundary layer separation points further upstream, and the reattachment points further downstream, increasing the volume occupied by the vortices within the aneurysm sacs. In the range of $500 < \mathrm{Re} \leq 2265$, however, the movement of the vortex center occurs towards the distal edge of each aneurysm, but not closer to the main stream. This results in a fairly constant core flow volume through the model for the higher flow rates (0.57 L/min $< Q \leq$ 2.59 L/min). For $\mathrm{Re} \geq 1750$, an induced secondary vortex is formed in the large aneurysm. This small vortex, which increases in size and intensity for Re = 2265, is clockwise-rotating, indicating the presence of positive wall velocity gradients. The formation of a second recirculation region, trapped between the AAA wall and the main vortex, occurs for a range of Reynolds numbers for which transition to turbulence has been observed experimentally. Therefore, an intermittent transition regime characterizes the results obtained for $1750 \leq \mathrm{Re} \leq 2265$.

The shear stress gradient distribution at the arterial wall is shown in Fig. 4. It is nondimensionalized by the *WSSG* obtained in a Poiseuille flow, $2\tau_{wo}/D$, for which D is the undilated diameter of the aorta. The peak *WSSG** in the small aneurysm is 6.40 times the shear stress gradient for an undilated aorta; similarly, the peak *WSSG** in the large aneurysm is 7.55 times the initial *WSSG*. A healthy aorta would then be exposed to focal variations of shear stress direction 10 times larger than those found in the center of an aneurysm. However, it is the distal end of an arterial expansion that experiences the high levels of *WSSG*. If individual endothelial cells are exposed to these levels of *WSSG*s when an aneurysm grows in an arterial branch, then the zero-tension hypothesis proposed by Lei and Kleinstreuer [31] for the mechanisms of cell response can be interpreted for a segment of an injured arterial wall in the following way: A normal, healthy endothelium maintains a non-zero state of stress, which is the result of its interaction with blood flow and blood's cellular components, causing axial and circumferential tension, normal stresses and shear stresses; for steady flow, a uniform shear stress field exists along the arterial wall. This results in a uniform but non-zero *WSSG* field (*WSSG** = 10 in Fig. 4), due to gradients of shear stress perpendicular to the wall. When this uniform *WSSG* field is disrupted as a consequence of deformities in the endothelium's geometry, levels of low and high gradients of shear stresses coexist within focal regions of the arterial wall. For low levels of *WSSG*s (*WSSG** < 10 in Fig. 4), disturbed flow conditions are diminished and the endothelium tries to regain its integrity at these locations. For high levels of *WSSG*s (*WSSG** > 10 in Fig. 4), there is a stronger viscous interaction at the wall, which promotes thrombus formation inside the aneurysm [34], further increasing the risk of rupture of the injured site.

Normal endothelial cells experience a non-zero intercellular tension condition, which exists under a uniform wall shear stress field and a zero *WSSG* [31]. However, while shear stress is constant at a healthy endothelium under steady flow conditions, there is a gradient of shear stress perpendicular to the wall. Since Eq. (39) defines the gradient of shear stress at the wall as a function of both $\partial\tau_w/\partial\hat{t}$ and $\partial\tau_w/\partial\hat{n}$, *WSSG* cannot be zero or negative, under normal conditions, even for quantification of cell responses.

4.1.3 Pulsatile flow. For pulsatile flow conditions, the inlet mean cross flow velocity is time-dependent and the volumetric flow rate has an oscillatory nature, as shown in Fig. 5. We represent the cardiac waveform by a discrete Fourier series based on twenty-six experimental points presented by Nazemi, et al. [35]. The time dependency of the mean cross flow velocity is imposed by the following Fourier representation:

$$\overline{u_m}(t) = A_0 + \sum_{k=1}^{N}\left(A_k \cdot \cos 2\pi kt + B_k \cdot \sin 2\pi kt\right) \tag{41}$$

where N = 8, the number of harmonics used. The natural frequency of the pulsatile waveform is set to $\omega = 2\pi$ rad/s, with a period $T_P = 1$ s, as shown in Fig. 5. The Womersley number, $\alpha = (D/2)\sqrt{\omega\nu}$, which characterizes the flow frequency, the geometry of the model and the fluid viscous properties, is $\alpha = 5.75$. The amplitude coefficient ($\beta = Re_{max}/Re_m$) of the flow is $\beta = 2.64$, and the peak systolic flow occurs at $t = 0.247$ s. The mean Reynolds number is calculated as $Re_m = D\overline{u_m}/\nu$, where ν is the blood kinematic viscosity, $\overline{u_m}$ is the time-average inflow mean velocity, from which $\overline{Q} = \pi(D^2/4)\overline{u_m}$, the time-average volumetric flow rate.

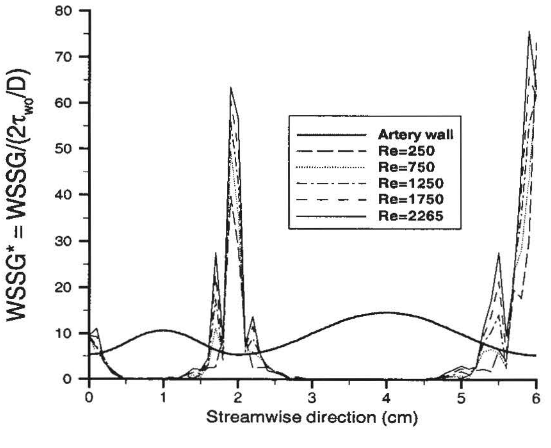

Figure 4 Distribution of nondimensional shear stress gradient along the wall of the two-aneurysm model.

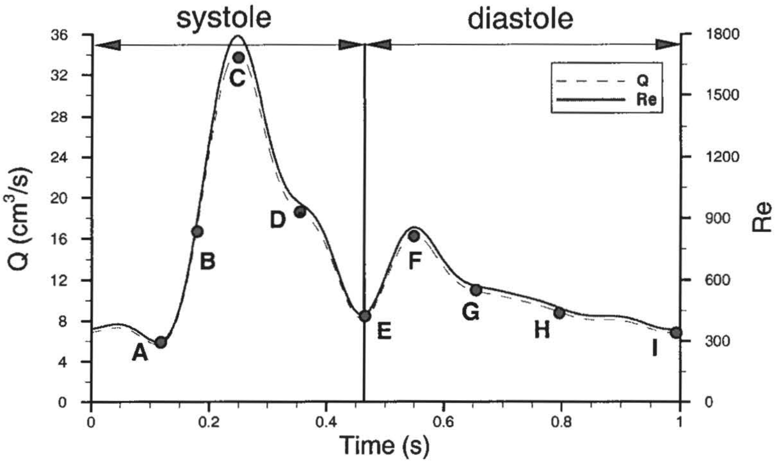

Figure 5 Pulsatile volumetric flow rate and Reynolds number for $Re_m = 680$. Flow stages A, B,..., I are of particular importance for the evaluation of hemodynamic parameters. Peak systolic flow occurs at t = 0.247 s and diastolic phase begins at $t = 0.465$ s.

Numerical simulations for pulsatile flow are performed at mean Reynolds numbers over the range $10 < Re_m < 680$. Re_m is defined as the time-average Reynolds number obtained by integrating the inlet Reynolds number over the pulsatile cycle. The instantaneous Reynolds number, $Re_i(t_j)$, is based on the spatially-averaged inlet velocity at time t_j. The pressure at the end of the two-aneurysm model is set to 70 mmHg, and all the pressure results presented are relative to this value. Results are obtained at 1/50 s intervals, but only selected flow stages considered to be the ones that represent the most important hemodynamic changes during the cycle are presented here. These stages are obtained at the last cycle of the asymptotically converged temporal solution, which is reached after a transient resulting from the application of the initial condition. Convergence is achieved when the flow becomes time periodic; this is verified by analyzing velocity plots at different points of the computational domain, as shown in Fig. 6 for $Re_m = 100$. For transient simulations, the initial value code solves the fully discrete set of governing equations at each time step by means of iterative solvers and tensor-product sum-factorization techniques.

The vortex dynamics induced by pulsatile blood flow in AAAs is characterized by means of a sequence of different flow stages in one period of the cardiac pulse. Figure 7 shows streamline plots for representative $Re_m = 680$ at nine flow stages in one cycle. The following five distinct flow phases depict the Reynolds-dependent and AAA-size-dependent vortex structures:

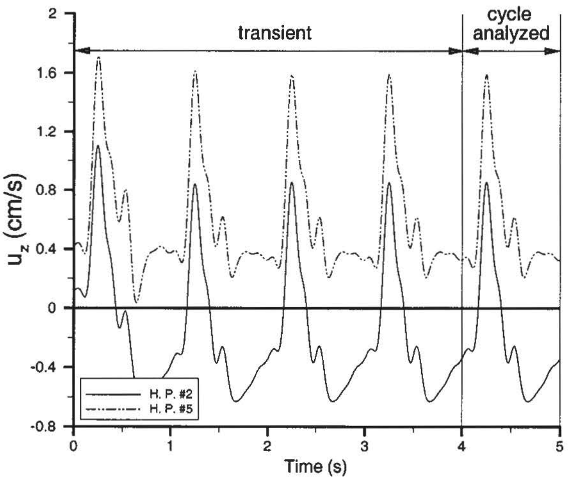

Figure 6 Temporal evolution of the axial velocity for $Re_m = 100$ at history points #2 and #5 (shown in Fig. 2) of the computational mesh.

(1) *Early systolic acceleration* which involves sweeping of vortices, left from the previous pulse, out of the deformed regions, resulting in an attached flow pattern. Vortices in the small AAA are swept earlier than in the large AAA.

(2) *Late systolic acceleration* is characterized by attached flow for low mean Reynolds numbers (Re_m). For high Re_m, the decrease in the temporal acceleration of the fluid upon reaching peak flow causes flow separation in the proximal ends of both aneurysms. The annular vortex forms earlier in the small AAA.

(3) *Systolic deceleration* is characterized by vortex growth and translation of vortex centers downstream. For high Re_m, secondary clockwise-rotating vortices are induced at the center of both aneurysms, once the main recirculation regions grow to full size. The end of systole itself is detailed as follows:

- For low Re_m, flow reattachment only occurs in the distal end of the large AAA.
- For moderate Re_m, the flow does not reattach to the wall.
- For high Re_m, the flow reattaches at the center of both AAAs, while the secondary vortices are trapped against the wall.

(4) *Early diastole*, during which partial sweeping of the vortex structures left from systole is obtained, driven by a favorable pressure gradient. The recirculation regions are reduced considerably in size, as the flow attempts to reattach to the wall.

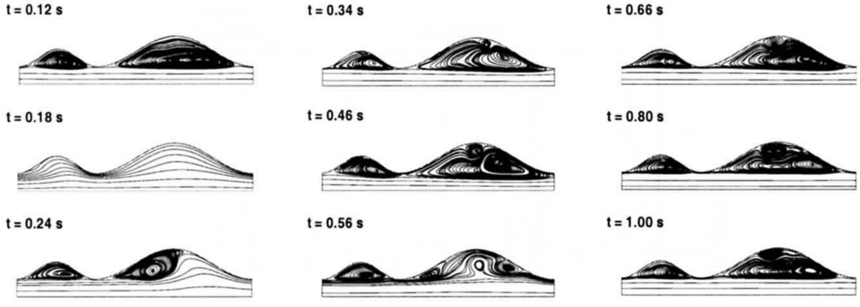

Figure 7 Streamlines for laminar pulsatile flow at $\mathrm{Re_m} = 680$. The direction of the flow is from left to right.

(5) *Late diastole* involves fairly constant full-size vortices within both AAAs, similar to a steady flow pattern. For high $\mathrm{Re_m}$, a secondary vortex coexists with the main recirculation region at the center of the large AAA.

In-vivo disturbed flow in localized regions of the cardiovascular system commonly subject to diagnosis of arterial diseases are typically associated with vortex structures, non-uniform fluid shear stress and high wall pressure. The focal occurrence of this hemodynamic disturbance has been correlated in-vitro with the alignment and migration of endothelial cells, as well as changes in their metabolic functions, which include cell division rates, protein-protein interactions, and cytosolic free calcium concentrations, among others. Non-uniform time-average shear stress measured experimentally at sites where irregular geometries take place in the arterial tree have led to the concept of shear stress gradient as a hemodynamic parameter of potential importance for explaining flow-induced arterial wall pathology and morphological changes in the endothelial lining. Therefore, we present the gradient of fluid shear stress evaluated in the tangential and normal directions to the arterial wall as a relevant hemodynamic force that influences the vortex dynamics of pulsatile blood flow in AAAs. The Wall Shear Stress Gradient (*WSSG*) distribution for $\mathrm{Re_m} = 680$ is shown in Fig. 8. The low, almost constant shear stress at the center of the AAA walls produces a constant *WSSG* of near-zero magnitude during the pulsatile cycle at these locations. At the proximal and distal ends of each aneurysm, however, the oscillatory behavior of the *WSSG* distribution is characterized by spatial variations at the sites where large velocity gradients occur. The regions where high positive and low negative shear stresses coexist due to flow reattachment are subjected to high *WSSG* values which are maximum at $t = 0.247$ s, when peak flow is obtained. High levels of *WSSG* are obtained in the small aneurysm during the accelerating phases of the cycle (early systole and early diastole), while the large aneurysm is subject to high *WSSG*s during the decelerating phases. This is explained by the fact that during temporal acceleration (consider $0.16\ \mathrm{s} \le t \le 0.22$ s, for example), vortex shedding and flow separation occurs earlier in the small aneurysm, producing higher shear stresses at the distal end. Alternatively, temporal deceleration induces secondary recirculation regions within the large aneurysm (e.g., 0.30 s $\le t \le$ 0.46 s), which result in an additional change of sign in the shear stress at the wall close to the point of flow reattachment. At peak values of flow rate where temporal acceleration is essentially zero (t = 0.247 s and t = 0.555 s), AAA size determines the magnitude of the shear stress distribution, resulting in higher *WSSG*s in the large aneurysm.

While the role of wall shear stress gradients in specific arterial diseases is not thoroughly understood yet, it is known that hemodynamic disturbance influences the endothelial lining of the cardiovascular system, and that the endothelium does not seem to be affected at an early stage of lesion development [36, 37]. Our numerical results for pulsatile flow point to an intermediate stage of AAA growth for which disturbed flow conditions exist. The quantification of this disturbance results in three distinct regions of flow development: (i) very low wall shear stresses at the center of an aneurysm; (ii) high wall shear stress gradients in the distal end of each AAA; and (iii) oscillating wall shear stresses and wall shear stress gradients at any site of the expanded arterial segment. The oscillatory nature of the *WSSG* at high mean volumetric flow rates, once the aneurysm has begun to grow, produces peak values of a periodic, pulsating hemodynamic force that may be responsible for severe sites of injury to the endothelium over a relatively long period of time.

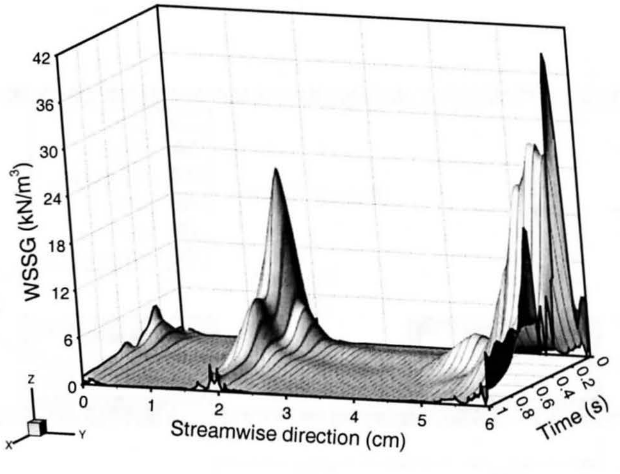

Figure 8 Wall Shear Stress Gradient (*WSSG*) distribution for Re_m = 680 as a function of time and axial location.

4.2 Heat Removal from Electronic Components: Convection-Only vs. Conjugate Conduction/Convection Predictions

The next application considers the heat removal by forced convection from surface-mounted electronic components on Printed Circuit Boards (PCBs). Figure 9 depicts a schematic of a periodic grooved-channel geometry with the configuration and material composition of the electronic components. Numerical simulations of the time-dependent convection-only and conjugate conduction/convection heat transfer are performed to ascertain the influence that conjugate effects have upon the convective heat transport. The conjugate results are contrasted with convection-only results obtained from simulating the fluid domain for the same geometry with uniform heat-flux boundary conditions along the grooved wall. The periodic grooved channels, formed by the electronic components and PCBs, are able to sustain Tollmien-Schlichting channel instabilities [38, 39]. The passive flow destabilization, induced by the spatially periodic disturbances introduced by the electronic components induces oscillatory flows, Tollmien-Schlichting traveling waves in the bypass region, and vortex ejections from the groove region which are flow mechanisms responsible for enhancing the overall mixing and, hence, improving the heat transfer performance [40]. Complex supercritical flow structure produces a time-repetitive sequence of convective exchange between the groove and the bypass regions. The periodic disruption of the shear layer coupled with the separation flow phenomenon at the downstream groove corner induces ejection of the hot fluid from the downstream component face into the bypass flow [18].

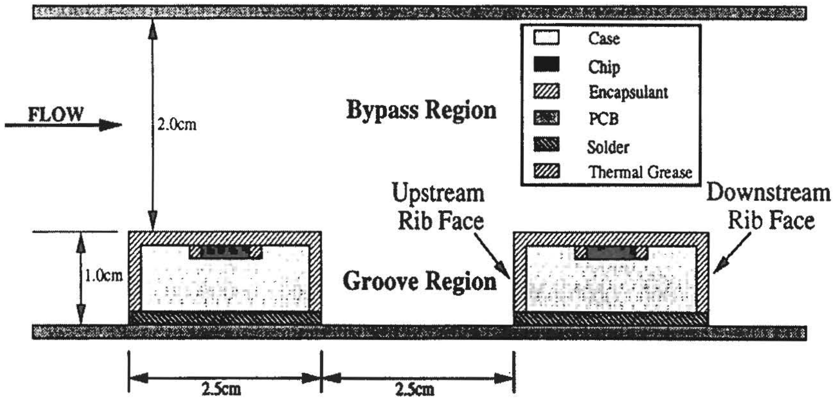

Figure 9 Schematic of the electronic component configuration and flow regions.

4.2.1 Convection simulations. We present first convection-only simulations where uniform heat flux at the solid-fluid interface is specified as the boundary condition. To satisfy this boundary condition, the wall temperature must adjust in accordance with the temperature of the fluid in the near-wall region of the boundary layer. Therefore, the temperature distribution along the wall is governed by a combination of the local fluid temperature and the wall shear stress, both being strongly related to upstream effects. The effect of the flow regime on the time-averaged difference between the surface and bulk-mean temperatures (ΔT) is presented in Fig 10. The distributions of ΔT along the top surface of the electronic component (rib) are quite similar for all the Reynolds numbers. However, the largest ΔT is exhibited by the near critical Reynolds number case (Re = 550), followed by the subcritical (Re = 261) and then the supercritical cases (Re = 600, 693). Within the subcritical flow regime the wake from the preceding rib is not fully homogenized. Therefore, the thermal boundary layer initiates with a finite thickness. As the boundary layer grows along the rib surface, its temperature increases to compensate for the energy diffused away from the wall. In the supercritical case, the wake is more completely homogenized, requiring a lower surface temperature at the leading edge of the rib to satisfy the constant flux boundary condition. Additionally, the supercritical bypass flow induces higher diffusion rates along the top surface of the rib, resulting in a more rapid increase in wall temperature than in the subcritical cases.

As the flow becomes supercritical, the ΔT is substantially reduced due to the transverse momentum and time-dependent nature of the supercritical bypass flow. In fact, all of the surfaces along the grooved wall experience a reduction in temperature. The waviness of the supercritical flow structure results in transverse convective transport, inducing large-scale mixing and a reduction of the effects associated with the wake.

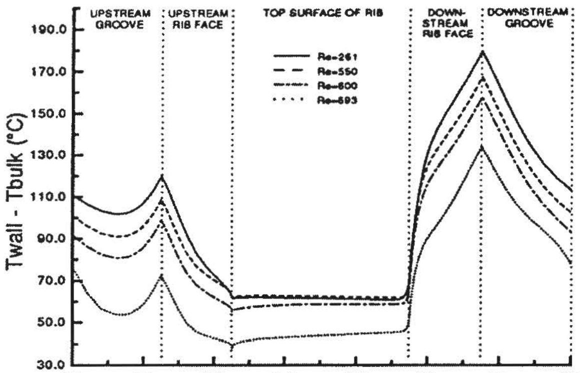

Figure 10 T_{wall} - T_{bulk} versus surface displacement for convection-only simulations.

The variations in convective behavior along the grooved surface can be visualized by examining the local distribution of the time-averaged Nusselt number, shown in Fig. 11, for Reynolds numbers Re in the subcritical (Re = 261) near critical (Re = 550) and supercritical (Re = 600, 693) flow regimes. Along the top surface of the rib, the Nusselt numbers decrease slightly with Reynolds number throughout the subcritical regime. However, this behavior reverses in the supercritical flow regime, as the Nusselt number increases significantly with Reynolds number. The Nusselt number within the groove region continuously increases with Reynolds number for both subcritical and supercritical flows, suggesting that the recirculating flow patterns within the groove significantly minimize any resistance associated with upstream effects.

In summary, the supercritical flow structure increases convective heat transport through three mechanisms. First, the traveling waves in the bypass region induce fluctuations in the velocity components. These fluctuations periodically increase the shear stress substantially above subscritical values, resulting in increased diffusion at the solid-fluid interface. Second, the supercritical bypass flow contains fluctuations in normal velocity, which partially homogenize the temperature distribution within the bypass flow and wake. Last, the supercritical flow structure disrupts the shear layer separating the groove and bypass flows. This disruption results in direct convective exchange between the groove and bypass flows, increasing surface transport rates. Therefore, the supercritical flow structure increase heat transport by both increasing diffusion at the solid-fluid interface and inducing large-scale mixing within and between the groove and bypass regions.

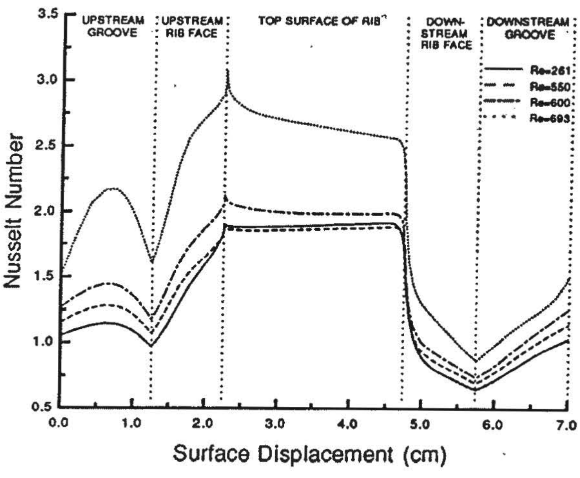

Figure 11 Time-averaged Nusselt number distribution along the grooved-channel wall, for subcritical and supercritical flows for convection simulations.

4.2.2 Conjugate conduction/convection simulations. In the conjugate conduction/convection simulations, heat is generated within the chip (Fig. 9), conducted through the electronic component and convected into the cooling fluid. The local flow characteristics in the grooved channel are the same as in the convection-only simulations with uniform heat-flux boundary conditions. However, the local thermal characteristics along with the composition and distribution of heat generation within the solid region dictate the local convective performance. Consequently, because of the additional internal heat resistances, in the electronic component, the surface temperature distribution (Fig. 12) exhibits a different pattern than in the convection-only simulations (Fig. 10). The concentrated heat generation in the chip produces a maximum ΔT directly above the location of the chip. This differs from the convection-only simulations in which the top surface of the rib displays the lowest ΔT and the groove surface the highest. In fact, for the conjugate case, the groove surface displays the lowest ΔT.

Contrary to the convection-only case, in conjugate conduction/convection, the ΔT increases from the subcritical to the supercritical flow regime, for the range of Reynolds numbers explored. In the convection-only case, the uniform flux boundary condition applied at the solid-fluid interface mandates that the product of the heat transfer coefficient and the temperature difference be constant. At supercritical Reynolds numbers, higher heat transfer coefficients result because of the combination of better flow homogenization and higher diffusive rates. Therefore, the ΔT must decrease to satisfy the uniform heat-flux boundary condition. However, the conjugate problem must satisfy a different boundary condition, namely continuity of flux and temperature at the solid-fluid interface.

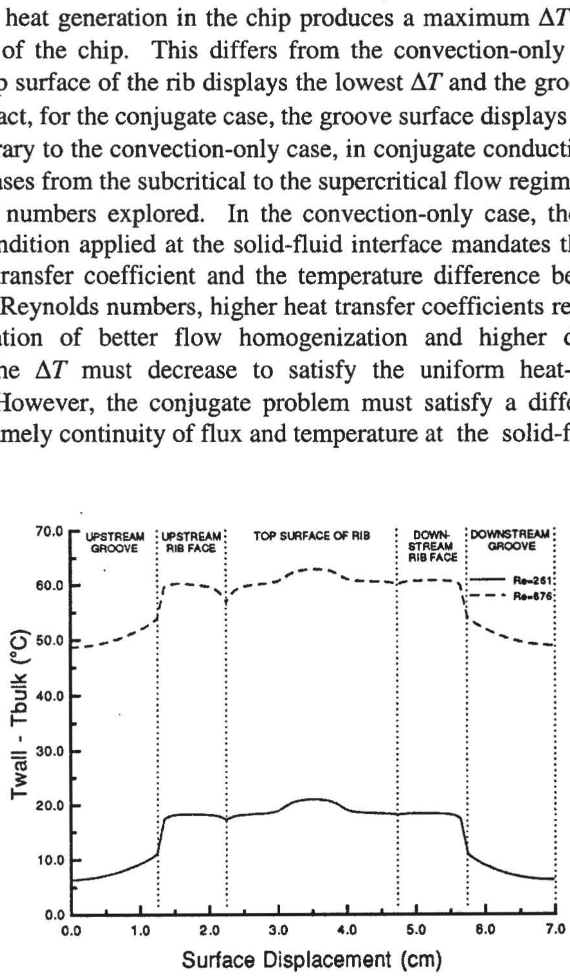

Figure 12 T_{wall} -T_{bulk} versus surface displacement for conjugate simulations.

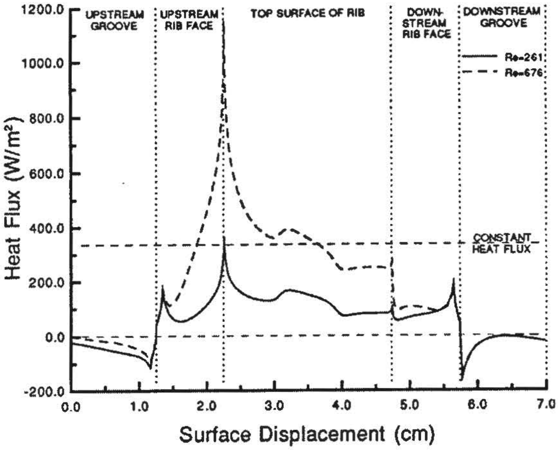

Figure 13 Time-averaged heat flux distribution along the solid-fluid interface for subcritical (Re = 261) and supercritical (Re = 676) flows for conjugate conduction/convection simulations, and constant heat.

As the Reynolds number increases within the range of this study, more heat is convected from the package surface (Fig. 13), causing larger internal temperature gradients. To satisfy the continuity of flux boundary condition, the temperature gradient within the fluid must similarly increase. Physically, as heat is removed from the package by the cooling fluid, the bulk temperature increases. Therefore, the surface temperature must likewise increase in order to maintain the temperature gradient at the solid-fluid interface.

The time-averaged heat flux distribution for the conjugate simulation is shown in Fig. 13 for subcritical (Re = 261) and supercritical (Re = 676) flow regimes. In the subcritical regime, the shear layer separating the groove and bypass flows precludes convective exchange of fluid. Therefore, the fluid recirculating within the groove, which is heated along the upstream and downstream component faces, becomes hotter than the local surface temperature at the groove bottom. This temperature gradient causes heat to be transferred from the fluid to the groove surface, producing negative heat fluxes in the upstream and downstream groove faces (Fig. 13). However, the bypass flow convectively cools the fluid within the groove when the shear layer is disrupted and the flow becomes supercritical and oscillatory. The heat flux distribution along the top surface of the rib is affected by the growth of the thermal boundary layer and the location of the heat generation, leading to an exponential decline in the downstream direction with a local rise directly over the location of the chip [18, 10]. Therefore, time-dependent forced convective transport phenomena, on complex, multimaterial solid domains with conjugate conduction/convection, exhibit different thermal performance than the one obtained by assuming uniform heat-flux boundary conditions. These results illustrate the importance of accounting for conjugate conduction/convection effects in the design and analysis of heat exchanger configurations such as those found in the cooling of electronic components.

4.3 Mass Transfer in Pulsating Flow Blood Oxygenators

For the final application, we consider three-dimensional simulations of pulsatile flows with oxygen transport. These simulations have been performed in the context of developing intravenous membrane oxygenators to complement the function of the natural lung for patients with the Acute Respiratory Distress Syndrome (ARDS). This is an illness that affects people's lungs characterized by a progressive interstitial edema, a diminished preliminary compliance and a decreased diffusion capability. Treatments based on mechanical ventilation, extracorporeal oxygenation and intravenous oxygenation have been developed with the goal of providing the patients with necessary respiratory support, until their lungs recover the normal gas exchange function [41-43]. Intravenous oxygenation is one of the treatments that have been proposed as a potentially attractive therapy in-patients with ARDS [44, 45]. The success of this treatment is based on its ability to reach levels of oxygen and carbon dioxide exchange appropriate for the metabolic requirements and make the intravenous oxygenation more clinically effective, without restricting cardiac return and seriously affecting the venous hemodynamics [44-46].

The Intravenous Membrane Oxygenator (IMO) device, shown in Fig. 14(a), is being currently tested at the University of Pittsburgh Artificial Lung program with the goal of reaching oxygen and carbon dioxide exchange of 50% of the metabolic requirements [45-47]. This device, which is inserted within the vena cava, has a centrally positioned elongated balloon within a bundle of hundreds of hollow fiber membranes. The balloon, made of elastic and non-permeable polyurethane walls, is inflated and deflated to a given amplitude and frequency by externally-pumped helium. The oxygen and carbon dioxide are transported longitudinally within the hollow fibers. The number of fibers within the IMO device varies between 700 and 1100 depending on the fiber size. Early in-vitro and in-vivo experiments [45-47] have indicated that balloon pulsation enhances IMO gas exchange by increasing fluid convection around the fiber bundle and that the additional convective flow depends on the amplitude and frequency of the balloon pulsations. In-vitro studies with a free fiber bundle, performed by Federspiel et al. [46], have shown that the critical frequency to maintain a sufficient oxygen flow rate and a good condition for volume amplitude of balloon pulsations is about 160 beats/min (bpm). The same experiments, performed in water, have shown that the gas exchange performance increases to an asymptotic stage as the pulsation frequency increases to 160 bpm. These results have allowed them to conclude that the pulsating balloon mechanism for enhancing convective mixing into the vena cava system most likely will be a key component to increase the efficiency of gas transfer at the fiber level. Recent in-vitro experiments by Federspiel et al. [48] with a constrained fiber bundle have indicated that this fiber configuration represents a better alternative in terms of pressure drop and gas exchange than the free fiber bundle. Guzmán and Amon [49, 50] have performed spectral element simulations and parametric investigations of the IMO device, to determine the flow mixing characteristics and mass transfer enhancement mechanisms induced by cross-pulsating blood flows, for both stationary and pulsating balloon conditions.

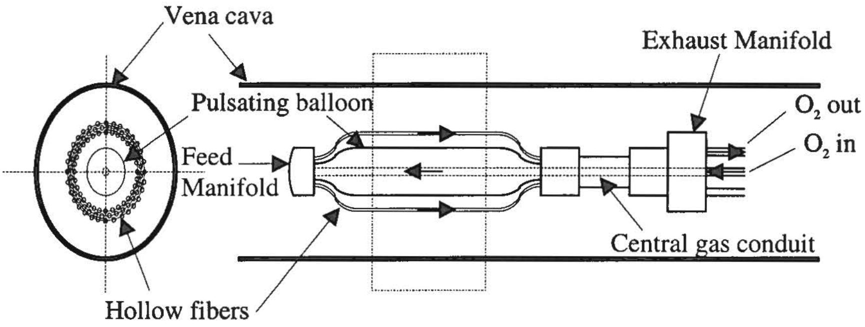

(a)

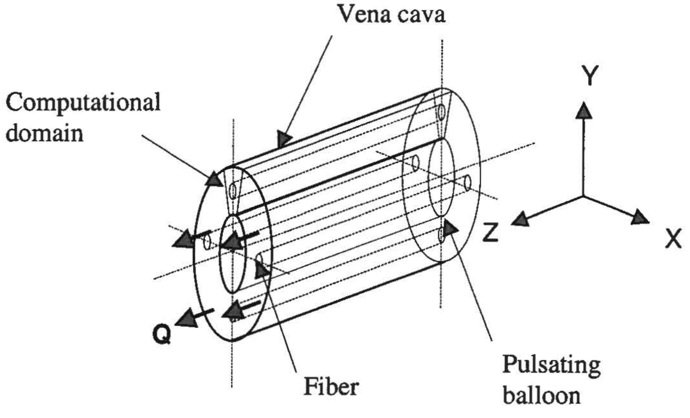

(b)

Figure 14 Intravenous Membrane Oxygenator (IMO) device: (a) schematic representation within the vena cava; and, (b) computational domain.

A schematic representation of the physical model of the IMO device is shown in Fig. 14(a), where for clarity, only a few fibers are shown. In the current simulations, the flow characteristics correspond to a hydrodynamically fully-developed flow regime. The three-dimensional (3D) computational model shown in Fig. 14(b) ignores inlet and exit geometric effects of the IMO device and assumes that the oxygen transport process occurs far from the feed and exhaust manifolds. This model also considers that the balloon inflates and deflates uniformly in the radial direction (i.e., normal to the surface balloon) and that the fibers remain stationary as in the in-vitro experiments, with their longitudinal axes parallel to the streamwise z-direction. The computational model assumes that there are 128 fibers uniformly distributed between the vena cava and balloon. Therefore, the physical space is divided into 128 regions of equal dimensions, where the flow and the oxygen transport characteristics repeat in each region. The computational domain is composed by one of these regions and is bounded by the physical boundaries of the vena cava, balloon and fiber, and by the fluid boundaries in the spanwise x- and streamwise z-directions. Notice that the streamwise length of this computational domain of $L = 4$ cm is shorter than the streamwise length (25 cm approximately) of the physical model.

The computational study considers a time-dependent, incompressible and Newtonian blood flow within the vena cava. For the operating conditions of a stationary balloon, the velocity field corresponds to a steady-state regime; whereas, for the pulsating balloon, the velocity field is time dependent because of the balloon motion. Two fundamental processes govern the oxygen transport mechanism: bulk convection and molecular diffusion. Oxygen is transported by the bulk convection in the blood that flows through the vessel and by molecular diffusion from the blood across vessel walls to the bulk flow. Almost all the oxygen is carried in reversible combination within the hemoglobin contained in the blood cells. In this study, the oxygen transport within the blood is described by a model of non-reacting species transport given by the conservation of species equation. Thus, the governing equations 1, 2 and 3(b), describe the blood flow and the oxygen transport within the Intravenous Membrane Oxygenator for the two operating conditions of this study: a stationary balloon and a pulsating balloon. Figure 15(a) shows the spectral element discretization of the computational domain; whereas, Figs. 15(b) and (c) illustrate mesh details and nodal points near the fiber surface where high velocity and oxygen concentration gradients are expected. The IMO model length is 4 cm, the fiber diameter is 250 μm and the vena cava diameter is 2.5 cm. Simulations performed with a stationary balloon consider the action of a streamwise pressure gradient only; whereas, for a pulsating balloon, a time-sinusoidal motion of the balloon wall along with the streamwise pressure gradient originates the flow. The balloon wall motion boundary condition defines a time-dependent computational domain problem [51].

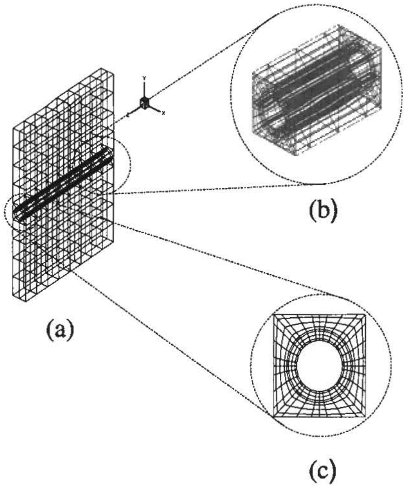

Figure 15 Spectral element discretization: (a) computational domain; (b) 3D macroelements close to the fiber; and, (c) collocation points.

Figures 16(a) and (b) show streamwise u_z-velocity profiles and velocity vector representations, respectively, for a stationary balloon condition in the Reynolds number range of Re = 5.7 - 455.2. The Reynolds number is defined as $\mathrm{Re} = D_{vc}\bar{u}/\nu$, where $\bar{u}$ is the mean velocity in the vena cava, D_{vc} is the vena cava diameter and ν is the kinematic viscosity. For successive increases of the Reynolds number the streamwise u_z-velocity profiles remain parabolic in shape between the vena cava and fiber and balloon wall. The only effect of the higher Re is to increase the mean velocity of the velocity profiles, but not its parabolic shape [49, 52].

For a stationary balloon, the vector representations show that the flow is parallel to the streamwise direction with absence of secondary flows and recirculation regions in the Reynolds number range of these simulations. Therefore, for a stationary balloon, the flow remains parallel, bi-directional, and parabolic in shape and without secondary flows. Figure 17 shows oxygen concentration profiles at the inlet of the computational domain, for the Reynolds numbers range of 5.7 - 455.2. Simulations have been performed with an oxygen concentration value of $c_w = 1.0\mathrm{x}10^{-5}$ ml-O_2/ml. The oxygen concentration profiles and their gradients at the fiber wall remain similar in shape and size as the Reynolds number increases. The oxygen concentration transport occurs very close to the fiber wall by a diffusion mechanism. The streamwise convection does not affect significantly the transport of oxygen to the bulk blood flow. Therefore, the oxygen diffusive mechanism to the blood flow saturates at relatively low Reynolds numbers. Thus, higher volumetric flow rates in the streamwise direction do not significantly increase the oxygen transport process efficiency [50, 51].

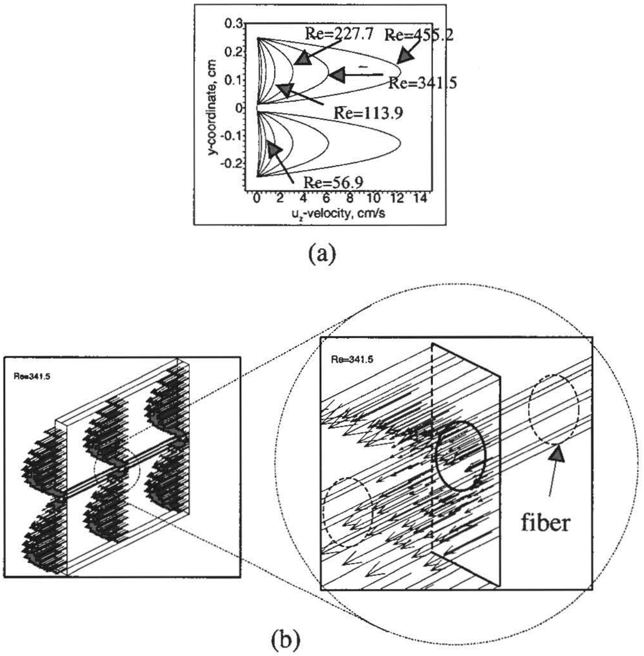

(a)

(b)

Figure 16 Velocity representation for a stationary balloon for the Reynolds number range of Re = 5.7 - 455.2: (a) streamwise u_z-velocity profiles; and, (b) velocity vectors and close up for Re = 341.5.

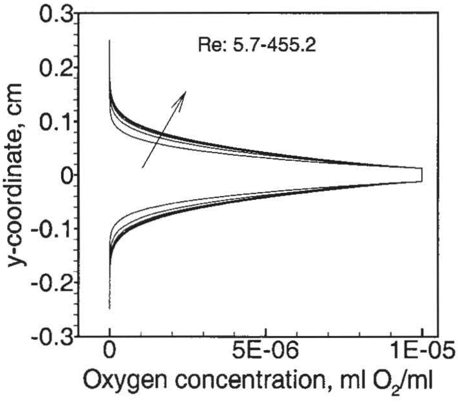

Figure 17 Oxygen concentration profiles for a stationary balloon for the Reynolds number range of Re = 5.7 - 455.2.

For a pulsating balloon condition, Fig. 18 shows velocity vector representations. In this type of simulation, the computational domain deforms continuously due to the pulsating balloon motion with no blood flow through the balloon wall. The balloon wall pulsates to a frequency of 60 beats/min (1 Hz) and a radial velocity of $u_y = 0.078539 \cdot \sin(2\pi 1t)$. The pulsating balloon originates a fluid motion that resembles the impaired oscillatory motion of the balloon wall. The magnitude of radial crosswise u_y-velocity below the fiber is larger than above the fiber because the fiber damps the radial flow and the momentum flux originated by the pulsating balloon. Around the fiber, the radial velocity increases in magnitude and accelerates the flow. Additionally, the pulsating balloon originates a secondary flow with a random spanwise velocity and a pulsatile streamwise velocity. This behavior increases the flow mixing, especially near the fiber and consequently increases the oxygen transport to the bulk flow [51, 52].

5 ACKNOWLEDGMENTS

The support of sponsors of this research, the National Science Foundation and The Whitaker Foundation, and the contributions of Ender Finol, Dr. Amador Guzmán and Dr. Jay Nigen are gratefully acknowledged. Some of the computations presented here have been performed at the PSC and NCSA Supercomputing Centers.

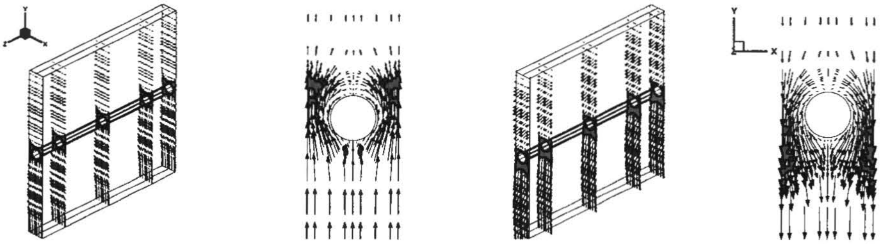

Figure 18 Instantaneous velocity vector representations for a pulsating balloon at two times of the sinusoidal balloon motion.

6 REFERENCES

1. C.H. Amon and B.B. Mikic, Computational Methodologies as a Research Tool in Complex Forced Convection Heat Transfer Systems: Present Status and Future Expectations, *Computers and Computing in Heat Transfer Science and Engineering*, CRC Press, Begell House, Boca Raton, FL, pp. 61-86, 1993.
2. W. Najayama and K.T. Yang, *Computers and Computing in Heat Transfer Science and Engineering*, CRC Press, Begell House, Boca Raton, FL, 1993.
3. I. Babuska and M.R. Dorr, *Numerical Mathematics*, Vol. 37, No. 2, pp. 257-277, 1981.
4. C. Canuto, M.Y. Hussaini, A. Quarteroni, and T.A. Zang, *Spectral Methods in Fluid Dynamics*, Springer-Verlag, New York, 1987.
5. J.P. Boyd, Chebyshev and Fourier Spectral Methods, *Lecture Notes in Engineering*, Springer-Verlag, Berlin, 1989.
6. A.T. Patera, A Spectral Element Method for Fluid Dynamics: Laminar Flow in a Channel Expansion, *Journal of Computational Physics*, Vol. 54, pp. 468-488, 1984.
7. C.H. Amon, Spectral Element-Fourier Method for Transitional Flow in Complex Geometries, *AIAA Journal*, Vol. 31, No. 1, pp. 42-48, 1993.
8. G.E. Karniadakis and R.D. Henderson, Spectral Element Methods for Incompressible Flows, *The Handbook of Fluid Dynamics*, CRC Press, pp. 29.1-29.41, 1998.
9. Y. Maday and A.T. Patera, Spectral Element Methods for the Navier-Stokes Equations, *ASME, State of the Art Surveys in Computational Mechanics*, 1987.
10. J.S. Nigen and C.H. Amon, Effect of Material Composition and Localized Heat Generation on Time-Dependent Conjugate Heat Transport, *International Journal of Heat and Mass Transfer*, Vol. 38, No. 9, pp. 1565-1576, 1995.
11. A.V. Luikov, Conjugate Convective Heat Transfer Problems," *International Journal of Heat and Mass Transfer*, Vol. 17, pp. 257-265, 1974.
12. A. Brosh, D. Degani and S. Zalmanovich, Conjugated Heat Transfer in a Laminar Boundary Layer with Heat Source at the Wall, *Journal of Heat Transfer*, Vol. 104, pp. 90-95, 1982.
13. K.D. Cole and J.V. Beck, Conjugated Heat Transfer from a Strip Heater with the Unsteady Surface Element Method, *Journal of Thermophysics and Heat Transfer*, Vol. 1, No. 4, pp. 348-354, 1987.
14. A. Campo and C. Schuler, Heat Transfer in Laminar Flow Through Circular Tubes Accounting for Two-Dimensional Wall Conduction, *International Journal of Heat and Mass Transfer*, Vol. 31, No. 11, pp. 2251-2259, 1988.

15. J.R. Culham, T.F. Lemczyk, S. Lee and M.M. Yovanovich, META — A Conjugate Heat Transfer Model for Air Cooling of Circuit Boards with Arbitrarily Located Heat Sources, *Heat Transfer in Electronic Equipment*, American Society of Mechanical Engineers-HTD, Vol. 171, pp. 117-126, 1991.
16. S. Ray and J. Srinivasan, Analysis of Conjugate Laminar Mixed Convection Cooling in a Shrouded Array of Electronic Components, *International Journal of Heat and Mass Transfer*, Vol. 35, No. 4, pp. 815-822, 1992.
17. J.S. Nigen and C.H. Amon, Conjugate Forced Convective Effects of Time Dependent Recirculating Flows in Grooved Channels, *Fundamentals of Forced Convection Heat Transfer*, edited by M.A. Ebadian and P.H. Oosthuizen, American Society of Mechanical Engineers-HTD, Vol. 210, pp. 91-98, 1992.
18. J.S. Nigen and C.H. Amon, Time-Dependent Conjugate Heat Transfer Characteristics of Self-Sustained Oscillatory Flows in a Grooved Channel, *Journal of Fluid Engineering*, Vol. 116, pp. 499-507, 1994.
19. M. Deville and S.A. Orszag, *Lecture Notes in Mathematics*, Vol. 771, Springer-Verlag, Berlin, 1980.
20. C.H. Amon, Heat Transfer Enhancement and Three-Dimensional Transition by a Spectral Element-Fourier Method, Sc.D. Thesis, Massachusetts Institute of Technology, Cambridge, MA, 1988.
21. G. Strang and G. Fix, An Analysis of the Finite Element Method, Prentice-Hall, Englewood Cliffs, NJ, 1973.
22. C. Ernst, Abdominal Aortic Aneurysm, *The New England Journal of Medicine*, Vol. 328, No. 16, pp. 1167-1172, 1993.
23. A.M. Guzmán and C.H. Amon, Dynamical Flow Characterization of Transitional and Chaotic Regimes in Converging-Diverging Channels, *Journal of Fluid Mechanics*, Vol. 321, pp. 25-57, 1996.
24. C.H. Amon, A.M. Guzmán, and B. Morel, Lagrangian Chaos, Eulerian Chaos, and Mixing Enhancement in Converging-Diverging Channel Flows, *Physics of Fluids*, Vol. 8, No. 5, pp. 1192-1206, 1996.
25. A.M. Guzmán, N.O. Moraga and C.H. Amon, Pulsatile Non-Newtonian Flow in a Double Aneurysm, *Proceedings of the 1997 ASME International Mechanical Engineering Congress and Exposition*, pp. 87-88, 1997a.
26. N.O. Moraga, A.M. Guzmán and C.E. Rosas, Mecánica de Fluidos No Newtonianos de Flujo Transiente en Tubería con Sección Transversal Variable en el Espacio, *VI Congreso La Ingeniería en la Industria del Cobre*, Universidad de Antofagasta, Chile, pp. 167-175, 1997.
27. A.M. Guzmán, N.O. Moraga, G. Muñoz and C.H. Amon, Pulsatile Non-Newtonian Flow in a Converging-Diverging Tube, *AIChE Symposium Series*, Vol. 93, No. 314, pp. 288-294, 1997b.
28. E. Finol and C. Amon, Blood Flow in Abdominal Aortic Aneurysms: The Two-Aneurysm Model, Part I – Steady Flow, *ASME Journal of Biomechanical Engineering*, 1999a, (to be published).

29. E. Finol and C. Amon, Blood Flow in Abdominal Aortic Aneurysms: The Two-Aneurysm Model, Part II – Pulsatile Flow, *ASME Journal of Biomechanical Engineering*, 1999b (to be published).
30. E. Albritton, Standard Values in Blood, *United States Air Force*. Wright Air Development Center, pp. 5-7, 1951.
31. M. Lei and C. Kleinstreuer, The Zero-Tension Hypothesis for the Mechanism of Atherogenesis and the Wall Shear Stress Gradient (*WSSG*) Predictor Equation, *Proceedings of the 1996 ASME International Mechanical Engineering Congress and Exposition*, pp. 211-212, 1996.
32. M. Lei, C. Kleinstreuer, and G. Truskey, Numerical Investigation and Prediction of Atherogenic Sites in Branching Arteries, *ASME Journal of Biomechanical Engineering*, Vol. 117, pp. 350-357, 1995.
33. C. Mills, I. Gabe, J. Gault, D. Mason, J. Ross Jr., E. Braunwald, and J. Shillingford, Pressure-Flow Relationships and Vascular Impedance in Man", *Cardiovascular Research*, Vol. 4, pp. 405-417, 1970.
34. D. Bluestein, L. Niu, R. Schoephoerster, and M. Dewanjee, Steady Flow in an Aneurysm Model: Correlation between Fluid Dynamics and Blood Platelet Deposition, *ASME Journal of Biomechanical Engineering*, Vol. 118, pp. 280-286, 1996.
35. M. Nazemi, C. Kleinstreuer and J. Archie Jr., Pulsatile Two-dimensional Flow and Plaque Formation in a Carotid Artery Bifurcation, *Journal of Biomechanics*, Vol. 23, No. 10, pp. 1031-1037, 1991.
36. R. Nerem, D. Harrison, R. Taylor, and R. Alexander, Hemodynamics and Vascular Endothelial Biology, *Journal of Cardiovascular Pharmacology*, Vol. 21, Suppl. 1, pp. S6-S10, 1993a.
37. R. Nerem, Hemodynamics and the Vascular Endothelium, *ASME Journal of Biomechanical Engineering*, Vol. 115, pp. 510-514, 1993b.
38. C.H. Amon, D. Majumdar, C.V. Herman, F. Mayinger, B.B. Mikic and D.P. Sekulic, Numerical and Experimental Studies of Self-Sustained Oscillatory Flows in Communicating Channels, *International Journal of Heat and Mass Transfer*, Vol. 35, No. 11, pp. 3115-3129, 1992.
39. C.H. Amon and A.T. Patera, Numerical Calculation of Stable Three-Dimensional Tertiary States in Grooved-Channel Flow, *Physics Fluids*, Vol. 1, No. 12, pp. 2005-2009, 1989.
40. C.H. Amon and B.B. Mikic, Numerical Prediction of Convective Heat Transfer in Self-Sustained Oscillatory Flows, *Journal of Thermophysics and Heat Transfer*, Vol. 4, No. 2, pp. 239-246, 1990.
41. K.M., High, M.T. Snider, R. Richard, G.B. Russell, J.K. Stene, D.B. Campbell, T.X. Aufiero, and G.A. Thieme, Clinical Trials of an Intravenous Oxygenator in Patients With Adult Respiratory Distress Syndrome," *Anesthesiology*, Vol. 77, pp. 856-863, 1992.
42. F.L. Fazzalari, R.H. Bartlett, M.R. Bonnell, and J.P. Montoya, An Intrapleural Lung Prosthesis: Rationale, Design, and Testing, *Artificial Organs*, Vol. 18, pp. 801-805, 1994.

43. S. Ichiba, and R.H. Bartlett, Current Status of Extracorporeal Membrane Oxygenation for Severe Respiratory Failure, *Artificial Organs*, Vol. 20, pp. 120-123, 1996.
44. J.D. Mortensen, Intravascular Oxygenator: A New Alternative Method for Augmenting Blood Gas Transfer in Patients With Acute Respiratory Failure, *Artificial Organs*, Vol. 16, pp. 75-82, 1992.
45. B.G. Hattler, P.C. Johnson, P.J. Sawzik, F.D. Shaffer, M. Klain, L.W. Lund, G.D. Reeder, F.R. Walters, J.S. Goode, and H.S. Borovetz, Respiratory Dialysis: A New Concept in Pulmonary Support, *American Society for Artificial Internal Organs Journal*, Vol. 38, pp. M322-M325, 1992.
46. W.J. Federspiel, T. Hewitt, M.S. Hout, F.R. Walters, L.W. Lund, P.J. Sawzik, G.D. Reeder, H.S. Boravetz, and B.G. Hattler, Recent Progress in Engineering The Pittsburgh Intravenous Membrane Oxygenator, *ASAIO Journal*, Vol. 42, 1996, pp. M435-M442.
47. B.G. Hattler, G.D. Reeder, P.J. Sawzik, L.W. Lund, F.R. Walters, A.S. Shah, J. Rawleigh, J.S. Goode, M. Klain, and H.S. Borovetz, Development of an Intravenous Membrane Oxygenator (IMO): Enhanced Intravenous Gas Exchange Through Convective Mixing of Blood Around Hollow Fiber Membranes, *Artificial Organs Journal,* Vol. 18, pp. 806-812, 1994.
48. W.J. Federspiel, M.S. Hout, T.J. Hewitt, L.W. Lund, S.A. Heinrich, P. Litwak, F.R. Walters, G.D. Reeder, H.S. Boravetz, and B.G. Hattler, Development of a Low Flow Resistance Intravenous Oxygenator, *ASAIO Journal*, Vol. 43, pp. M725-M730, 1997.
49. A.M. Guzmán, and C.H. Amon, Mass Transfer Performance Evaluations of an Intravenous Membrane Oxygenator, *Proc. of the 1998 ASME International Mechanical Engineering Conference and Exposition*, HTD-Vol. 362; BED-Vol. 40, *Advances in Heat and Mass Transfer in Biotechnology*, S. Clegg (Ed.) pp. 149-154, 1998.
50. A.M. Guzmán, and C.H. Amon, Flow and Mass Transfer Characteristics of an Intravenous Membrane Oxygenator: A Computational Study, *Journal of Computer Methods in Biomechanics and Biomedical Engineering*, 1999, in press.
51. A.M. Guzmán, and C.H. Amon, Mass Transfer Enhancement in an Intravenous Membrane Oxygenator Induced by a Pulsating Balloon, *1999 ASME International Mechanical Engineering Conference and Exposition*, Nashville, TN, November 1999.
52. A.M. Guzmán, C.H. Amon, W.J. Federspiel, and B.G. Hattler, Spectral-Element Simulations of the Flow Kinematics in an Intravenous Membrane Oxygenator, *Proc. of the Fourth World Congress on Computational Mechanics*, Vol. 2, p. 1011. Also published in *Computational Mechanics, New Trends and Applications*, pp. 1-14, Idelsohn, Onate & Dvorkin (Eds.), CIMNE, 1998.